

Geometric Static Modeling Framework for Piecewise-Continuous Curved-Link Multi Point-of-Contact Tensegrity Robots

Lauren Ervin and Vishesh Vikas¹

Abstract—Tensegrities synergistically combine tensile (cable) and rigid (link) elements to achieve structural integrity, making them lightweight, packable, and impact resistant. Consequently, they have high potential for locomotion in unstructured environments. This research presents geometric modeling of a Tensegrity eXploratory Robot (TeXploR) comprised of two semi-circular, curved links held together by 12 prestressed cables and actuated with an internal mass shifting along each link. This design allows for efficient rolling with stability (e.g., tip-over on an incline). However, the unique design poses static and dynamic modeling challenges given the discontinuous nature of the semi-circular, curved links, two changing points of contact with the surface plane, and instantaneous movement of the masses along the links. The robot is modeled using a geometric approach where the holonomic constraints confirm the experimentally observed four-state hybrid system, proving TeXploR rolls along one link while pivoting about the end of the other. It also identifies the quasi-static state transition boundaries that enable a continuous change in the robot states via internal mass shifting. This is the first time in literature a non-spherical two-point contact system is kinematically and geometrically modeled. Furthermore, the static solutions are closed-form and do not require numerical exploration of the solution. The MATLAB® simulations are experimentally validated on a tetherless prototype with mean absolute error of 4.36°.

I. INTRODUCTION

Robot locomotion in non-uniform terrains is a requirement for applications of space, search and rescue, and agriculture. Wheeled robots provide efficient and reliable locomotion in structured environments through continuity of contact with the surface. Their adaptation for unstructured environments include integration of legs [1] and introduction of discontinuity with compliance [2], [3]. Additionally, spherical robots have garnered interest due to the unique rolling locomotion and ability to rebound from collisions [4]–[6]. The curved-link tensegrity robot presented in this research brings together the best of both worlds - discontinuities in wheel-designs, and locomotion ability of spherical robots.

The term of tensegrity was introduced in the 1960s by Fuller and Snelson with initial applications in architecture [7]. Fundamentally, it combines rigid links under compression with prestressed cables held in tension to achieve structural integrity. As a result, they are lightweight, packable,

and do not rely on gravity to maintain structural integrity [8]. Mobile tensegrity robots aim to leverage these advantages for locomotion in unstructured environments. Commonly, these robots are based on tensegrity primitives comprised of two, three, six, and 12 rigid, straight-links [9]–[11]. Locomotion with straight-links is discrete and results from shape change achieved by altering cable or link lengths [12]. Vibration-based locomotion has also been explored by Rieffel et al [13].

In contrast, curved link robots adapt the rolling motion of a spheres to enabling energy efficient locomotion [14]–[17]. For example, the two curved-link (2CL) robot [15] is about three times faster (normalized to body lengths/min) than the fastest straight-link counterpart. Here, the momentum change is achieved through internal mass shifting. This actuation methodology provides a greater ability of manipulating the momentum, while keeping the number of actuators low, i.e., one moving mass per link opposed to linear actuators along cables and links. The presented research adopts a similar conceptual design. Despite the design advantages, the modeling of such a two-point contact system with piecewise continuity of the curved links remains a challenge. For example, Böhm et al [16] modeled the system where it is assumed that the robot performs uniaxial rolling about one end of the curved link and the internal mass moves along a separate straight line connecting the two ends of a link. However, this non-geometric approach makes an assumption that the robot pivots about the end of one link and rolls along the another, does not consider the masses of the curved links, and the model is qualitatively validated. Kaufhold et al [17] experimentally study the toppling locomotion of this robot where there is change in the point of pivot. Schorr et al [18] also use Euler angles approach to modeling the kinematics of a three curved-link robot capable of shape morphing. In short, this approach, while effective, faces challenges with generalization and scaling, and also does not provide insight into the hybrid nature of the robot that is experimentally observed. Antali et al [19] propose an approach to model of two point of contact locomotion of a sphere along two orthogonal planes similar to the edge of a wall. This paper addresses the mentioned shortcomings by adopting an elegant, generalizable, and scalable geometric modeling approach that proves the hybrid state of the robot and is experimentally validated.

Contributions. The paper statically models a mobile, curved-link tensegrity robot using a geometric representation and provides subsequent simulation and validation. The generalizable modeling framework is adaptable to robots with

*The material contained in this document is based upon work supported in part by a National Aeronautics and Space Administration (NASA) grant or cooperative agreement. Any opinions, findings, conclusions, or recommendations expressed in this material are those of the authors and do not necessarily reflect the views of NASA. This work was supported through a NASA grant awarded to the Alabama/NASA Space Grant Consortium.

¹Lauren Ervin and Vishesh Vikas are with the Agile Robotics Lab, University of Alabama, Tuscaloosa, AL 35487, USA lefaris@crimson.ua.edu, vvikas@ua.edu

multiple points of contact and different morphologies. The model analytically proves the hybrid nature of the system where the robot exists in four states. Each state corresponds to the motion where the robot instantaneously pivots about the end of one curved link and rolls along the other. Static simulations provide input-output relationship between the internal mass position and ground contact points, equivalently, the robot orientation. A tetherless robot prototype experimentally validates the static model with high accuracy.

Paper Organization The next section explores the kinematics of the robot and proves the hybrid nature of the system. The static modeling is analyzed in the following section. Thereafter, the fabrication and design methodology of the tensegrity robot is presented. Next, simulations with a scenario of state change along the transition boundaries for a quasi-static control path and real-world experimental results are discussed. The final section concludes the research and explores the future directions.

II. ROBOT KINEMATICS

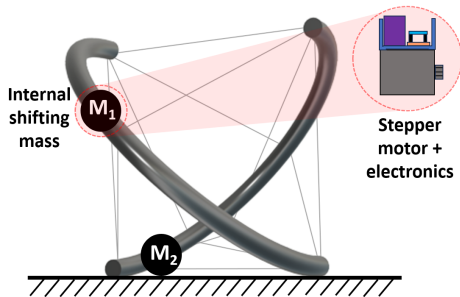


Fig. 1: Two curved-link tensegrity robot, TeXploR, is structurally held together with 12 tensile cables. Change of robot pose is achieved through internal masses shifting along the curved links. At any instant in time, it has two points of contact with the ground.

A. Problem definition and notation

The Tensegrity eXploratory Robot (TeXploR), Fig. 1, comprises of two curved-links held together with a tensile cable with two motor assemblies that are free to move along the links. The two links, $\{L_1, L_2\}$, are modeled as semi-circular arcs with radii r with masses $\{m_1, m_2\}$, Fig. 2. The two endpoints of the two arcs are denoted as $\{A_i, B_i\}$ for link L_i . For the remainder of this section, $i = 1, 2$ corresponding to the two links. The body coordinate system $\{b\}$ is fixed on the robot body with origin O_b and orthonormal basis $U_b = [\mathbf{x}_b, \mathbf{y}_b, \mathbf{z}_b] \in SO(3)$. Let coordinate systems $\{1, 2\}$ be fixed on the corresponding link with origin at the center of each arc, such that the x and z axes respectively are along the arc end points $B_i A_i$, and normal to the arc plane. The center of the two links are coincident and $\{1\}$ coincides with $\{b\}$. The inertial coordinate system $\{s\}$ is fixed at origin O_s with orthonormal basis $U_s = [\mathbf{x}_s, \mathbf{y}_s, \mathbf{z}_s] \in SO(3)$ such that \mathbf{z}_s is normal to the plane of locomotion. The motor assemblies are modeled as point masses M_i that move along

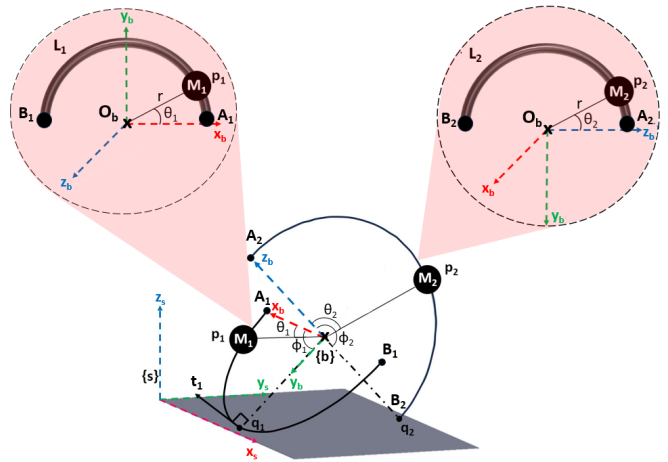


Fig. 2: Geometric relationship the spatial $\{s\}$, body $\{b\}$ and link $\{1\}, \{2\}$ coordinate systems. Here, $\{b\}, \{1\}$ coincide and \mathbf{z}_s is the normal to the surface of locomotion. The internal masses P_i and ground contact points Q_i along the links are denoted using θ_i, ϕ_i respectively where $i = 1, 2$. The tangents \mathbf{t}_i at the contact points lie along the surface.

the corresponding link. These point masses P_i are defined using angle θ_i from \mathbf{x}_i and denoted by $\mathbf{p}_i \in \mathbb{R}^{3 \times 1}$. The instantaneous points of contact, Q_i , between the links and the ground plane are represented by $\mathbf{q}_i \in \mathbb{R}^{3 \times 1}$ and parameterized using ground contact angles ϕ_i from \mathbf{x}_i . The tangents of the arc at these instantaneous points of contact are denoted by $\mathbf{t}_i \in \mathbb{R}^{3 \times 1}$. Terminology of the shifting masses and points of contact is summarized in Tab. I.

TABLE I: Shifting Masses and Points of Contact

Motor $i = 1, 2$			Point of contact $i = 1, 2$	
\mathbf{p}_i	Position of motor i	\mathbf{q}_i	Link i	
θ_i	Angle along motor	ϕ_i	Angle link i	
M_i	Shifting mass	\mathbf{t}_i	Tangent line i	
r	Arc radius	R_{12}	Rotation matrix b/w $\{1\}, \{2\}$	
A_1, B_1	Arc 1 endpoints	A_2, B_2	Arc 2 endpoints	

Ultimately, it is desired to find the transformation matrix $T_{sb} \in SE(3)$, such that

$$T_{sb} = \begin{bmatrix} R_{sb} & \mathbf{o}_{sb} \\ \mathbf{0}_{3 \times 1} & 1 \end{bmatrix} \quad (1)$$

where $R_{sb} \in SO(3)$, \mathbf{o}_{sb} are the rotation matrix and displacement between origins of $\{s\}, \{b\}$.

B. Kinematics

The position vectors $\mathbf{p}_i, \mathbf{q}_i$ are represented as a combination of the arc radius and respective angles along arcs.

$$\mathbf{p}_i^i = r \begin{bmatrix} c\theta_i \\ s\theta_i \\ 0 \end{bmatrix}, \quad \mathbf{q}_i^i = r \begin{bmatrix} c\phi_i \\ s\phi_i \\ 0 \end{bmatrix} \quad (2)$$

where $c_{\alpha_i} = \cos(\alpha_i), s_{\alpha_i} = \sin(\alpha_i), \forall i = 1, 2, \alpha = \theta, \phi$, and the superscript i refers to the c.s. of representation. The

transformation matrix $T_{12} \in SE(3)$ changes the representation between c.s. $\{2\}$ to $\{1\}$. That is, for some vector $\mathbf{v} \in \mathbb{R}^{3 \times 1}$

$$\begin{aligned} \begin{bmatrix} \mathbf{v}^1 \\ 1 \end{bmatrix} &= T_{12} \begin{bmatrix} \mathbf{v}^2 \\ 1 \end{bmatrix} \Rightarrow \mathbf{v}^1 = \mathbf{o}_{12}^1 + R_{12} \mathbf{v}^2 \\ T_{12} &= \begin{bmatrix} R_{12} & \mathbf{o}_{12}^1 \\ \mathbf{0}_{1 \times 3} & 1 \end{bmatrix}, R_{12} = \begin{bmatrix} 0 & 0 & 1 \\ 0 & -1 & 0 \\ 1 & 0 & 0 \end{bmatrix}, \mathbf{o}_{12}^1 = \begin{bmatrix} 0 \\ 0 \\ 0 \end{bmatrix} \end{aligned} \quad (3)$$

where $R_{12} \in SO(3)$ and $\mathbf{o}_{12} \in \mathbb{R}^{3 \times 1}$ are the rotation matrix and the displacement between the origins of the $\{1\}, \{2\}$. For the remainder of the paper, we disregard the superscript for the vector notation, as all the representations will be in the robot body c.s. $\{b\}$ which coincides with $\{1\}$. Hence,

$$\begin{aligned} \mathbf{p}_1 &= r \begin{bmatrix} c\theta_1 \\ s\theta_1 \\ 0 \end{bmatrix}, \quad \mathbf{p}_2 = \mathbf{o}_{12} + R_{12} \mathbf{p}_2^2 = r \begin{bmatrix} 0 \\ -s\theta_2 \\ c\theta_2 \end{bmatrix} \\ \mathbf{q}_1 &= r \begin{bmatrix} c\phi_1 \\ s\phi_1 \\ 0 \end{bmatrix}, \quad \mathbf{q}_2 = \mathbf{o}_{12} + R_{12} \mathbf{q}_2^2 = r \begin{bmatrix} 0 \\ -s\phi_2 \\ c\phi_2 \end{bmatrix} \end{aligned} \quad (4)$$

The ‘free-vector’ tangent \mathbf{t}_i at points of contact Q_i are

$$\mathbf{t}_i = \frac{\partial \mathbf{q}_i}{\partial \phi_i} \quad (5)$$

C. Rolling constraint

Pure rolling without slipping is assumed at the points of contact, Q_1, Q_2 . Hence, they have zero velocity, i.e., $\dot{\mathbf{q}}_1 = \dot{\mathbf{q}}_2 = 0$. We use the Lie group approach for modeling and follow the notation as per [20]. The body twist, $\xi_b \in \mathbb{R}^6$, encodes the angular velocity ω_b and linear velocity of the origin O_b , v_b expressed in $\{b\}$. The hat operator $\hat{\cdot}$ maps $\mathbb{R}^{6 \times 1} \rightarrow \mathfrak{se}(3)$ and $\mathbb{R}^{3 \times 1} \rightarrow \mathfrak{so}(3)$

$$\xi_b = \begin{bmatrix} \omega_b \\ v_b \end{bmatrix}, \quad \hat{\xi}_b = \begin{bmatrix} \hat{\omega}_b & v_b \\ 0 & 0 \end{bmatrix} \in \mathfrak{se}(3)$$

Following this notation, the rolling constraint is

$$\dot{\mathbf{q}}_i = v_b + \hat{\omega}_b \mathbf{q}_i = 0$$

In this paper, we restrict ourselves to static analysis and do not examine this constraint given the modeling complexity, especially, the hybrid nature of such two-point contact system to be discussed next.

D. Holonomic constraint

It is assumed that the robot is in physical contact with the surface of locomotion at all times. This implies that the two points Q_1, Q_2 are in contact with the ground and the tangents at those points also lie on the ground plane. The ground plane is defined using the surface normal which is the z -axis \mathbf{z}_s of $\{s\}$. Another kinematic interpretation of this is that the \mathbf{z}_s component of position \mathbf{q}_i is the minimum amongst all the points on the link. For the two points of contact Q_i

$$[\mathbf{z}_s^T, 1] \cdot \left(T_{sb} \begin{bmatrix} \mathbf{q}_i \\ 1 \end{bmatrix} \right) = 0, \quad [\mathbf{z}_s^T, 1] \cdot \left(T_{sb} \begin{bmatrix} \mathbf{t}_i \\ 0 \end{bmatrix} \right) = 0 \quad (6)$$

This can be simplified to

$$\begin{bmatrix} (\mathbf{q}_1 - \mathbf{q}_2)^T \\ (\mathbf{t}_1)^T \\ (\mathbf{t}_2)^T \end{bmatrix} \mathbf{z}_b = \mathbf{0}, \quad \mathbf{z}_b = R_{sb}^T \mathbf{z}_s, \quad \text{s.t.} \quad \mathbf{z}_s = \begin{bmatrix} 0 \\ 0 \\ 1 \end{bmatrix} \quad (7)$$

Geometrically, this implies that vectors $(\mathbf{q}_1 - \mathbf{q}_2), \mathbf{t}_1, \mathbf{t}_2$ lie in the same plane and the vector \mathbf{z}_b is the surface normal. However, there is discontinuity at the edges of the links, i.e., $\phi_i = 0, 180^\circ$ where the tangents cannot be defined. These discontinuities can be separated into three unique cases:

Case 1: Tangent vector \mathbf{t}_2 not defined. Here, vector \mathbf{z}_b is normal to the vector $Q_1 Q_2$ and tangent vector at Q_1 . The direction of \mathbf{z}_b can be deduced from the fact that \mathbf{o}_{sb} , origin O_b of $\{b\}$ lies above the ground plane, i.e., $\mathbf{z}_s^T \mathbf{o}_{sb} > 0$, and Q_1, Q_2 are in contact with the ground. Mathematically,

$$\mathbf{z}_s^T (\mathbf{o}_{sb} + R_{sb} \mathbf{q}_i) = 0, \quad \text{and} \quad \mathbf{z}_s^T \mathbf{o}_{sb} > 0 \Rightarrow -\underbrace{(R_{sb}^T \mathbf{z}_s)^T}_{\mathbf{z}_b^T} \mathbf{q}_i > 0$$

The analytical solution for \mathbf{z}_b can then be summarized as

$$\begin{aligned} \mathbf{z}_b &= \pm \frac{\mathbf{t}_1 \times (\mathbf{q}_1 - \mathbf{q}_2)}{|\mathbf{t}_1 \times (\mathbf{q}_1 - \mathbf{q}_2)|} \quad \text{s.t.} \quad -\mathbf{z}_b^T \mathbf{q}_1 = -\mathbf{z}_b^T \mathbf{q}_2 > 0 \\ \mathbf{z}_b &= -\frac{1}{\sqrt{2}} [c\phi_1, s\phi_1, c\phi_2]^T, \quad -\mathbf{z}_b^T \mathbf{q}_1 = -\mathbf{z}_b^T \mathbf{q}_2 = \frac{r}{\sqrt{2}} \end{aligned} \quad (8)$$

Case 2: Tangent vector \mathbf{t}_1 not defined. Similar to the previous case, \mathbf{z}_b is normal to the vector $Q_1 Q_2$ and the tangent vector at Q_2 . Using the surface-contact constraint, the analytical expression of unique \mathbf{z}_b is

$$\begin{aligned} \mathbf{z}_b &= \pm \frac{\mathbf{t}_2 \times (\mathbf{q}_2 - \mathbf{q}_1)}{|\mathbf{t}_2 \times (\mathbf{q}_2 - \mathbf{q}_1)|} \quad \text{s.t.} \quad -\mathbf{z}_b^T \mathbf{q}_1 = -\mathbf{z}_b^T \mathbf{q}_2 > 0 \\ \mathbf{z}_b &= \frac{1}{\sqrt{2}} [-c\phi_1, s\phi_2, -c\phi_2]^T, \quad -\mathbf{z}_b^T \mathbf{q}_1 = -\mathbf{z}_b^T \mathbf{q}_2 = \frac{r}{\sqrt{2}} \end{aligned} \quad (9)$$

Case 3: Both tangent vectors \mathbf{t}_i defined. For this case, \mathbf{z}_b is normal to the plane containing vector $Q_1 Q_2$ and tangent vectors at both points Q_1 and Q_2 . Consequently, the angles ϕ_i can be analytically written as

$$\begin{aligned} (\mathbf{q}_1 - \mathbf{q}_2)^T (\mathbf{t}_1 \times \mathbf{t}_2) &= 0 \\ \Rightarrow -r^3 (s\phi_1 + s\phi_2) &= 0 \Rightarrow \phi_2 = -\phi_1 \text{ or } 180^\circ + \phi_2 \\ \mathbf{z}_b &= \frac{\mathbf{t}_1 \times \mathbf{t}_2}{|\mathbf{t}_1 \times \mathbf{t}_2|} \\ \phi_2 &= \begin{cases} -\phi_1, & \mathbf{z}_b = \frac{1}{\sqrt{2c_{\phi_1}^2 + s_{\phi_1}^2}} [c\phi_1, s\phi_1, c\phi_1]^T \\ 180^\circ + \phi_1, & \mathbf{z}_b = \frac{1}{\sqrt{2c_{\phi_1}^2 + s_{\phi_1}^2}} [c\phi_1, s\phi_1, -c\phi_1]^T \end{cases} \end{aligned} \quad (10)$$

This case is infeasible due to the range constraints on ϕ_1, ϕ_2 . More specifically, for $\phi_2 > 0$, both $-\phi_1$ and $180^\circ + \phi_1$ are outside of the solution space, i.e., the arc range $\phi_2 \in [0, 180^\circ]$.

E. Hybrid system

Given that the surface normal is defined only for cases 1 and 2, the robot can be modeled as a hybrid system transitioning between four states. Each case corresponds to the robot instantaneously pivoting about one of the end points of the curved link.

- State 1:** $\phi_1 \in (0, 180^\circ), \phi_2 = 0^\circ$, A_2 pivot, roll along L_1
State 2: $\phi_1 \in (0, 180^\circ), \phi_2 = 180^\circ$, B_2 pivot, roll along L_1
State 3: $\phi_1 = 0^\circ, \phi_2 \in (0, 180^\circ)$, A_1 pivot, roll along L_2
State 4: $\phi_1 = 180^\circ, \phi_2 \in (0, 180^\circ)$, B_1 pivot, roll along L_2

As an example, the geometric representation of the robot in State 2 and pivoting about the link end point B_2 where tangent vector \mathbf{t}_2 is not defined is shown in Fig. 2. The robot is a hybrid system transitions between four states of locomotion. More importantly, all the states are not connected to each other. For example, the robot cannot transition directly from State 1 to 2, instead the transition is $1 \rightarrow 3 \rightarrow 2$ or $1 \rightarrow 4 \rightarrow 2$. In each of these states, the transition occurs when ϕ_i is fixed at $0^\circ, 180^\circ$ and $\dot{\phi}_{i\pm 1} > 0$. The hybrid state system is summarized in Fig. 3.

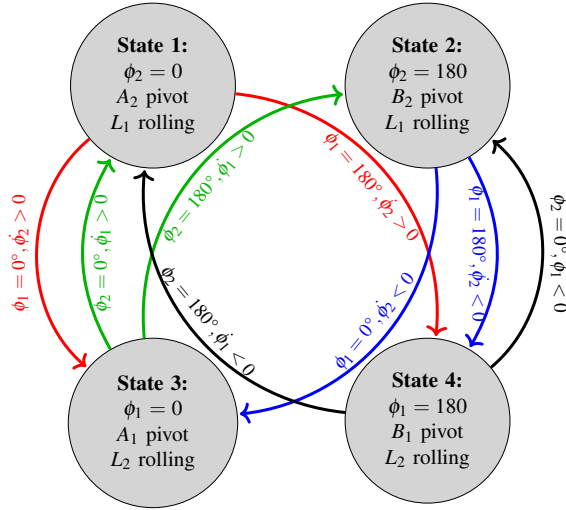


Fig. 3: Four state hybrid system model of the TeXploR. The state transition is decided by the pivot and the rate of change of point of contact $\dot{\phi}_i$. During each state, the robot pivots about one of the ends of the curved links while rolling about the other.

Let's analyze the transition between States $1 \rightarrow 3 \rightarrow 2 \rightarrow 4$. While in State 1, ϕ_1 reaches the end of L_1 , point A_1 . The robot transitions to State 3 as $\phi_1 \rightarrow 0^\circ$ and pivots about A_1 while ϕ_2 begins to traverse the entirety of L_2 . Next, it arrives at the $\phi_2 = 180^\circ$, i.e., B_2 . Now, with $\dot{\phi}_1 > 0$, and the robot transitions to State 2. Here, $\phi_2 = 180^\circ$ as $\phi_1 \in (0^\circ, 180^\circ)$ traverses L_1 , stopping at the B_1 . Finally, it transitions to State 4. The robot repeatedly transitions between these four states either forwards or backwards for a rolling sequence.

F. Generalizability for different robot morphologies

The extension of this framework to different curved-link tensegrity morphologies will require it to be applied to systems with variations in robot shape, i.e., T_{12} , number of curved links, length of the curved links.

Shape morphing. The variations in cable tensions have direct impact on the robot shape, more specifically, the transformation matrix T_{12} as defined in (3). It has been documented that variations in the orientation and distance between the two curved links has direct impact on the rolling

locomotion path [17]. For this research, the curved links are orthogonal with coincident arc centers. This enables a straight trajectory of locomotion during a rolling sequence. Shape morphing of the robot, reflected in T_{12} and shown in Fig. 4(a), will allow the robot to turn. This change can be incorporated by updating the point of contact Q_2 and the tangent vector as a function of \mathbf{o}_{12}, R_{12} .

$$\mathbf{q}_2 = \mathbf{o}_{12} + R_{12}\mathbf{q}_2^2, \quad \mathbf{t}_2 = \frac{\partial \mathbf{q}_2}{\partial \phi_2}$$

Number of curved links. The framework is adaptable to tensegrity robots with more curved links, e.g., three as shown in Fig. 4(b). For this morphology, (7) will be modified to

$$[(\mathbf{q}_1 - \mathbf{q}_2) \quad (\mathbf{q}_2 - \mathbf{q}_3) \quad (\mathbf{t}_1) \quad (\mathbf{t}_2) \quad (\mathbf{t}_3)]^T \mathbf{z}_b = \mathbf{0} \quad (11)$$

where $\mathbf{q}_3, \mathbf{t}_3$ are defined for the new point of contact Q_3 on the third curved link. Consequently, the analysis will result in a change in number of robot states in the hybrid system.

Curve link length. The arc lengths of the curves can be varied beyond 180° as illustrated in Fig. 4(c). This alteration in the robot morphology will result in reconsideration of the possibility of a solution existing for 'Case 3' discussed in Sec. II-D. This may result in an increase in the number of robot states from the four discussed earlier.

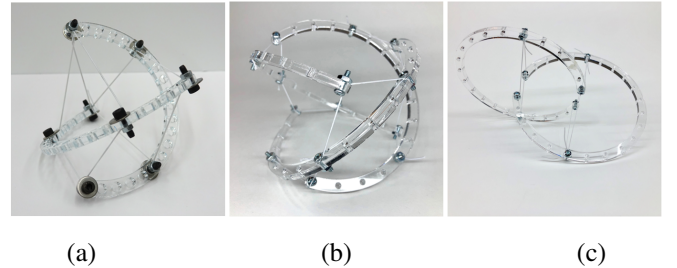


Fig. 4: Different robot morphologies that can be modeled with the generalizable framework: (a) A two link prototype with a different shape and T_{12} . (b) A three curved-links resulting in three points of ground contact. (c) A two link prototype with arc length more than 180° .

III. STATIC MODELING

The two-point of contact and hybrid nature of the system results in a robot existing in four states. Consequently, the analytical solution to the statics problem is obtained by equating the wrench to zero and solving for the unique point of ground contact corresponding to the robot orientation.

A. Closed form solution for point of contact

The wrench, \mathcal{F} , is comprised of the total force, f , and moment, m , acting on the body. For the static formulation, the wrench \mathcal{F} about O_b is equated to zero. The corresponding free body diagram of the two point of contact system showing all forces is shown in Fig. 5. Here, the center of mass of the curved links $\mathbf{r}_1 = \mathbf{r}_2 = [0, 2r/\pi, 0]^T$.

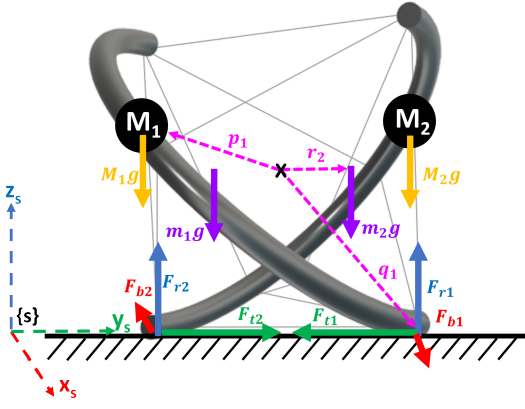


Fig. 5: The free-body diagram of TeXploR with the inertial and reaction forces.

$$f = \begin{bmatrix} F_{b1} - F_{b2} \\ F_{r1} - F_{r2} \\ (M_1 + M_2 + m_1 + m_2)g - (F_{r1} + F_{r2}) \end{bmatrix}$$

$$m = (M_1 g \hat{p}_1 + M_2 g \hat{p}_2 + m_1 g \hat{r}_1 + m_2 g \hat{r}_2 - F_{r1} \hat{q}_1 - F_{r2} \hat{q}_2) \mathbf{z}_b + (F_{b1} \hat{q}_1 - F_{b2} \hat{q}_2) \mathbf{x}_b + (F_{r1} \hat{q}_1 - F_{r2} \hat{q}_2) \mathbf{y}_b$$

These are six equations with seven unknowns F_{bi}, F_{ti}, F_{ri} and ϕ_i along the rolling link for the corresponding state. These can be simplified to four equations with three unknowns F_{r1}, F_{r2}, ϕ_i by observing that $F_{b1} = F_{b2}, F_{r1} = F_{r2}$, and $Q_1 Q_2$ lies in the same plane as $\mathbf{x}_s, \mathbf{y}_s$, i.e., $(\hat{q}_1 - \hat{q}_2) \mathbf{x}_b = (\hat{q}_1 - \hat{q}_2) \mathbf{y}_b = 0$. Hence,

$$\begin{bmatrix} (M_1 + M_2 + m_1 + m_2)g - (F_{r1} + F_{r2}) \\ (M_1 g \hat{p}_1 + M_2 g \hat{p}_2 + m_1 g \hat{r}_1 + m_2 g \hat{r}_2 - F_{r1} \hat{q}_1 - F_{r2} \hat{q}_2) \mathbf{z}_b \end{bmatrix} = 0$$

Using the calculated \mathbf{z}_b from Sec. II-D for each state, the ground contact angles and the reaction forces are analytically determined as

State 1: Pivot about A_2 ($\phi_2 = 0^\circ$), rolling on L_1

$$\mathbf{z}_b = -\frac{1}{\sqrt{2}} [c_{\phi_1}, s_{\phi_1}, 1]^T, \quad \tan \phi_1 = \frac{s_{\theta_1} - s_{\theta_2}}{c_{\theta_1}}$$

$$F_{r1} = Mg \left[-1 + \frac{c_{\phi_1 + \theta_2}}{2} - c_{\theta_2} + c_{\phi_1 - \theta_1} - \frac{c_{\phi_1 - \theta_2}}{2} \right] - mg$$

$$F_{r2} = Mg \left[-1 - \frac{c_{\phi_1 + \theta_2}}{2} + c_{\theta_2} - c_{\phi_1 - \theta_1} + \frac{c_{\phi_1 - \theta_2}}{2} \right] - mg \quad (12)$$

State 2: Pivot about B_2 ($\phi_2 = 180^\circ$), rolling on L_1

$$\mathbf{z}_b = -\frac{1}{\sqrt{2}} [c_{\phi_1}, s_{\phi_1}, 1]^T, \quad \tan \phi_1 = \frac{s_{\theta_1} - s_{\theta_2}}{c_{\theta_1}}$$

$$F_{r1} = Mg \left[-1 + \frac{c_{\phi_1 + \theta_2}}{2} + c_{\theta_2} + c_{\phi_1 - \theta_1} - \frac{c_{\phi_1 - \theta_2}}{2} \right] - mg$$

$$F_{r2} = Mg \left[-1 - \frac{c_{\phi_1 + \theta_2}}{2} - c_{\theta_2} - c_{\phi_1 - \theta_1} + \frac{c_{\phi_1 - \theta_2}}{2} \right] - mg \quad (13)$$

State 3: Pivot on A_1 ($\phi_1 = 0^\circ$), rolling about L_2 :

$$\mathbf{z}_b = \frac{1}{\sqrt{2}} [-1, s_{\phi_2}, -c_{\phi_2}]^T, \quad \tan \phi_2 = \frac{s_{\theta_2} - s_{\theta_1}}{c_{\theta_2}}$$

$$F_{r1} = Mg \left[-1 - \frac{c_{\phi_2 + \theta_1}}{2} + c_{\theta_1} - c_{\phi_2 - \theta_2} + \frac{c_{\phi_2 - \theta_1}}{2} \right] - mg$$

$$F_{r2} = Mg \left[-1 + \frac{c_{\phi_2 + \theta_1}}{2} - c_{\theta_1} + c_{\phi_2 - \theta_2} - \frac{c_{\phi_2 - \theta_1}}{2} \right] - mg \quad (14)$$

State 4: Pivot on A_2 ($\phi_1 = 180^\circ$), rolling about L_2 :

$$\mathbf{z}_b = \frac{1}{\sqrt{2}} [-1, -s_{\phi_2}, c_{\phi_2}]^T, \quad \tan \phi_2 = \frac{s_{\theta_2} - s_{\theta_1}}{c_{\theta_2}}$$

$$F_{r1} = Mg \left[-1 - \frac{c_{\phi_2 + \theta_1}}{2} + c_{\theta_1} - c_{\phi_2 - \theta_2} + \frac{c_{\phi_2 - \theta_1}}{2} \right] - mg$$

$$F_{r2} = Mg \left[-1 + \frac{c_{\phi_2 + \theta_1}}{2} - c_{\theta_1} + c_{\phi_2 - \theta_2} - \frac{c_{\phi_2 - \theta_1}}{2} \right] - mg \quad (15)$$

B. Rotation matrix

As evident, the static analysis allows for closed form solution for \mathbf{z}_b . The equilibrium orientation does not provide any information about the planar position of the robot on the surface, i.e., x, y components of O_b are ‘free’ while the z component is fixed at $r/\sqrt{2}$ as calculated in (8),(9). Hence, ignoring additional rotation about \mathbf{z}_s the rotation matrix can be calculated using the Rodrigues’ formula and vectors $\mathbf{z}_s, \mathbf{z}_b$

$$R_{sb}(\mathbf{u}, \theta) = I + \sin \theta \hat{\mathbf{u}} + (1 - \cos \theta) \hat{\mathbf{u}}^2$$

$$\text{where } \mathbf{u} = \frac{\mathbf{z}_b \times \mathbf{z}_s}{|\mathbf{z}_b \times \mathbf{z}_s|}, \quad \theta = \text{atan2}(|\mathbf{z}_b \times \mathbf{z}_s|, \mathbf{z}_b^T \mathbf{z}_s) \quad (16)$$

Rodrigues’ formula is used to convert the axis \mathbf{u} and rotation angle θ into a rotation matrix in $SO(3)$. Additionally, $\mathbf{o}_{sb}^s = x, y, \sqrt{r}/2]^T$ for some x, y , i.e., the robot can sit anywhere on the plane. A closed form solution for T_{sb} can be obtained by using the calculated R_{sb} and \mathbf{o}_{sb} .

IV. TEXPLORER DESIGN AND FABRICATION

A. Static form finding

The robot is a tensegrity mechanism that combines elements of tension and compression. The shape of the robot, T_{12} , depends upon the cable segment lengths. Form-finding determines the lengths that dictate a desired shape. These can be found by minimizing the energy of the system [21], [22]. We define the problem in terms of the generalized coordinates, i.e., the screw ξ using a Lie groups approach. The four connection points on each curved link are identical and expressed in the corresponding link coordinate systems. Consequently, the 12 cable segments are expressed as $\mathbf{d} \in \mathbb{R}^{12 \times 4}$ and the i th cable \mathbf{d}_i is denoted by the i th row

$$\mathbf{d}(\xi) = PC_1 - e^{\hat{\xi}} PC_2 = PC_1 - T_{12} PC_2$$

$$P = \begin{bmatrix} \mathbf{p}_A & \mathbf{p}_B & \mathbf{p}_C & \mathbf{p}_D \\ 1 & 1 & 1 & 1 \end{bmatrix} = \begin{bmatrix} -r & 0 & 0 & 1 \\ \frac{-r}{2} & \frac{-\sqrt{3}r}{2} & 0 & 1 \\ \frac{r}{2} & \frac{\sqrt{3}r}{2} & 0 & 1 \\ r & 0 & 0 & 1 \end{bmatrix}^T \quad (17)$$

where P are the concatenated homogeneous representation of points A, B, C, D on each arc, and the Fig. 6. The connectivity matrices C_1, C_2 mathematically represent the two end-points each cable

$$C_i[j, k] = \begin{cases} 1, & \text{if cable } k \text{ contains vertex } j \text{ on link } i \\ 0, & \text{otherwise} \end{cases}$$

Now, the energy minimization problem can be written as

$$\xi^* = \min_{\xi} \sum_{i=1}^{12} \frac{1}{2} k_i (|\mathbf{d}_i| - d_{0,i})^2 \quad (18)$$

where $k_i, d_{0,i}$ are the stiffness and the free length of the corresponding cable. There are two different free length cable segments in the system corresponding to edge-to-edge and edge-to-middle segments, $d_{0,1} = 3.25''$ and $d_{0,2} = 3''$. The optimal $T_{12} = e^{\frac{5}{2}}$ corresponding to the free-length matches (3) where $d_1 = 5.8551, d_2 = 5.5412$, visualized in Fig. 6(a).

B. Tendon routing

Routing the cable through the two arcs such that the mechanism maintains structural integrity is challenging given the antagonistic nature of tensile cables and compressive rigid curved links. This is achieved by finding the Euler path of the graph where the connected edges and vertices correspond to the cables and connection points respectively. The reader may refer to [23] for more details. One such Euler path, $A_1 \rightarrow C_2 \rightarrow B_1 \rightarrow D_2 \rightarrow A_1 \rightarrow B_2 \rightarrow C_1 \rightarrow A_2 \rightarrow D_1 \rightarrow B_2 \rightarrow B_1 \rightarrow A_2 \rightarrow A_1$, is shown in Fig. 6(b). Here, the sequence simplifies the fabrication process by ensuring the cable traverses each edge only once. Once routed, the segments are tightened until the two curved links are held in tension with the optimal cable lengths identified through form-finding.

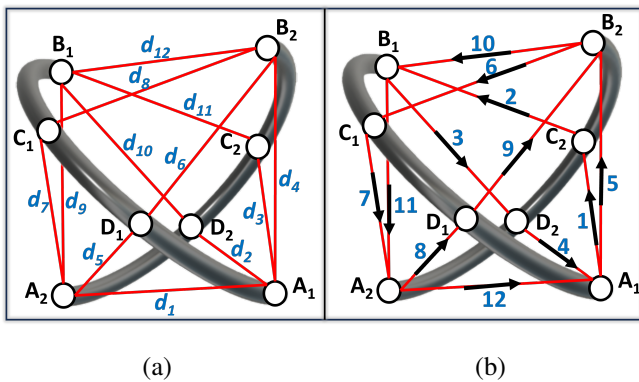


Fig. 6: (a) The twelve cables joining different points on the two curved links are denoted by $d_j, j \in [1, 12]$. (b) The tendon routing path $A_1 \rightarrow C_2 \rightarrow B_1 \rightarrow D_2 \rightarrow A_1 \rightarrow B_2 \rightarrow C_1 \rightarrow A_2 \rightarrow D_1 \rightarrow B_2 \rightarrow B_1 \rightarrow A_2 \rightarrow A_1$ ensures that each edge is only traversed once.

C. Mechatronics

TeXploR is comprised of two 3D printed tough PLA curved links with 83mm thickness and 403mm diameter that are structurally held together with a cable using the discussed form-finding and routing approach. Motion is performed with a motor assembly traversing a GT2 timing belt running along the inside curvature of the arc. A side view of an open arc with the traveling motor assembly is shown in Fig. 7. The motor and electronic components are all positioned to one side of the timing belt with supporting delrin sliders on the top and side to maintain track alignment during movement. An Arduino Nano33 IoT, A4988 motor driver, 1,100mAh LiPo battery, and PCB are arranged compactly atop the traveling NEMA17 stepper motor. The assembly is designed with matching arc topology to reduce surface friction. Each

semicircular arc weighs 431g and while each shifting mass weighs 427g, resulting in a nearly 1:1 weight ratio. The high ratio allows incremental movements of the masses to have a larger impact on the overall shifting center of mass.

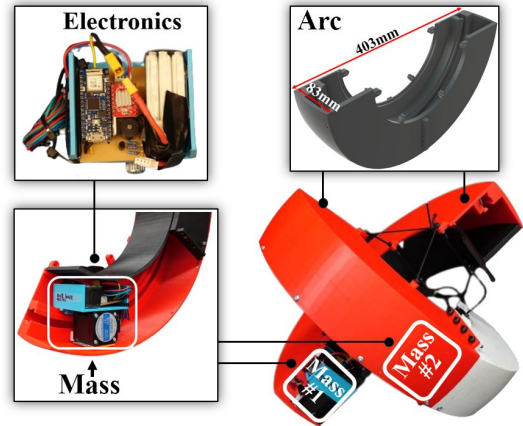


Fig. 7: TeXploR comprises of two arcs with 83mm thickness and 403mm diameter. The internal shifting masses (mechanics) that move along a GT2 belt internal to each arc.

V. RESULTS

A. Simulation

Simulations are performed in MATLAB® to obtain the equilibrium position of the robot. Given the positions of the internal masses (θ_1, θ_2), the equilibrium position can be interpreted as the two points of contacts represented through ground contact angles (ϕ_1, ϕ_2). These four states of the robot are analytically found using (12)-(15). As an example, Fig. 8 illustrates the four state solutions for internal mass positions $(\theta_1, \theta_2) = (45^\circ, 90^\circ)$. Here, the black cross, pink squares and blue circles indicates the origin O_b of the body coordinate system, internal masses and points of contact with the ground respectively.

The simulated ground contact angles for the four states as a function of the internal mass positions are shown in Fig. 9. As evident from the analytical solutions, the ground contact angles for States (1, 2) and (3, 4) solutions are identical. The plots demarcate the solutions in four distinct quadrants separated by the state transition boundaries highlighted by the dotted red lines in State 2 of Fig. 9. When considering this state, the bottom and top quadrants result in more movement of the robot, i.e., greater change in ϕ_2 for change in (θ_1, θ_2) as compared to the left and right quadrants. The state transition boundaries represent the internal mass positions where the robot can switch states. Consider two movement sequences visualized in Fig. 9 to highlight this phenomenon. The robot starts at internal mass position $x_0 = (0, 0)$ of State 1. Next, the internal masses are quasi-statically moved to position x_1 where ϕ_2 is fixed at 0° . Thereafter, the robot travels along a vertical path (θ_1 constant, θ_2 increasing) and approaches the state transition boundary where $\phi_1 \rightarrow 0^\circ$. Instantaneously the robot enters the left quadrant of State 3 and ϕ_1 begins to increase, and rolls to position x_2 . The

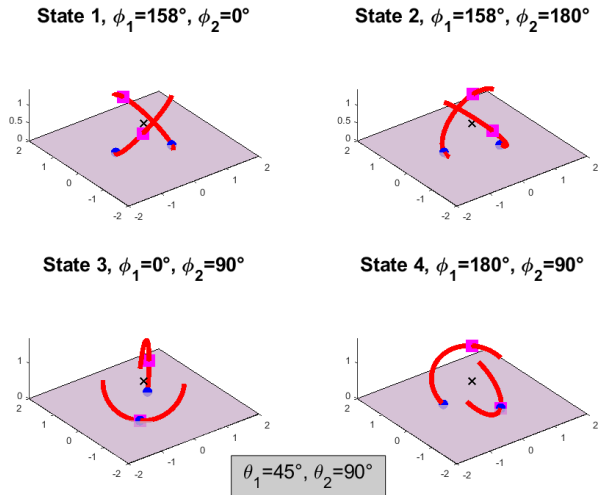


Fig. 8: Four static equilibrium solutions for $(\theta_1 = 45^\circ, \theta_2 = 90^\circ)$. The blue dots are the points of contact q_i , the pink squares are the positions of the internal masses p_i , and the black ‘x’ represents origin O_b of the body coordinate system.

second movement again starts with the robot at position x_0 in State 1 rolling to x_1 , and then begins to move towards the right state transition boundary as $\phi_1 \rightarrow 180^\circ$. The robot transitions along the boundary and instantly enters the right quadrant of State 4, stopping at x_3 .

B. Real-world experiments

The prototype described in Sec. IV is used for experimental validation of the simulations. For combination of (θ_1, θ_2) in increments of 45° , the ground contact angles (ϕ_1, ϕ_2) corresponding to the robot orientation were observed. Protractor strips were attached along the curved links for observing the angles. All results were compared with simulation for each state in Fig. 10(a). For most of the inputs, the ϕ_i angles match exactly. The mean absolute error (MAE) over all the inputs is 4.36° . The factors contributing to these differences between real-to-sim can be attributed to the assumptions and simplifications in the model of the system. More specifically, the curved links are modeled as 2D bars with a single ground contact point, however, the prototype has an arc thickness of 83mm with a curved arc endpoint allowing for a range of different ground contact points. Additionally, the center of mass of each shifting mass is modeled as a point mass while the mechatronics of the shifting mass are not centered due to uneven component layout. For example, the LiPo battery is attached to one side and weighs approximately a sixth of the total shifting mass. The experimental results for each input for State 1 are shown in Fig. 10(b).

VI. CONCLUSIONS

This research introduces a static modeling framework using geometric representation applicable to multi-point of contact systems. Here, the holonomic constraints prove the hybrid nature of the piecewise continuous rolling robot which exists in four states. Such multi-point contact system

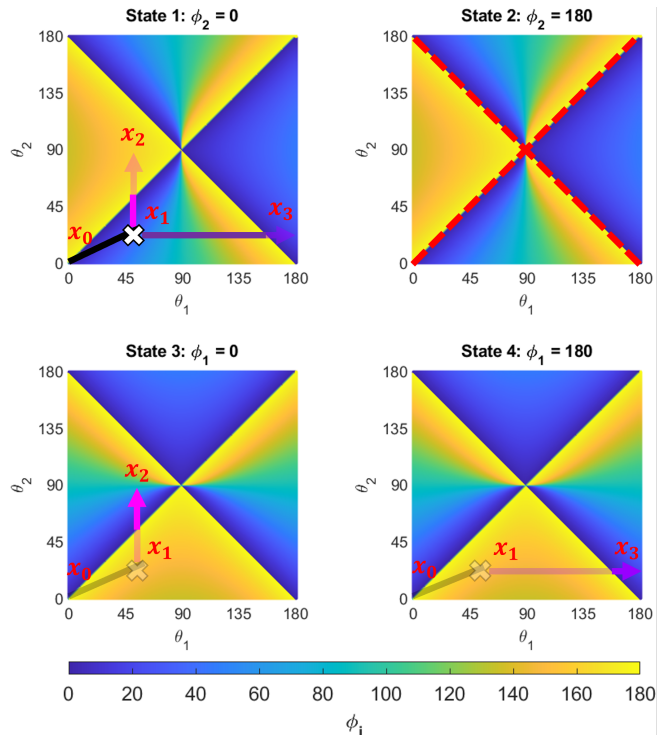


Fig. 9: Simulation of static equilibrium positions of the four states. Two quasi-static control path sequences highlight the state transition boundaries (dotted red line): $x_0 \rightarrow x_1 \rightarrow x_2$ for State 1 \rightarrow 3 and $x_0 \rightarrow x_1 \rightarrow x_3$ for State 1 \rightarrow 4.

modeling has been explored for the first time in literature and the hybrid state model is verified by the real-world behavior of the robot. Each state physically corresponds to one of the end points of the two curved links about which the robot pivots while rolling along the other link. The modeling framework is generalizable and extendable to similar platforms of varying morphologies, i.e., robots with different shape, greater number of curved links, and varying curved link length, or their combination. The static analysis yields a four quadrant relationship between internal mass positions and ground contact angles. The quadrants are separated by state transition boundaries. Here, a quasi-static movement along these boundaries will result in change of states, i.e., physical change in the pivot points. The model is validated on a physical tetherless prototype with a MAE of 4.36° , highlighting the accuracy of the model.

The future work involves dynamically modeling the TeXploR with consideration of dynamic movement of the internal mass. This will include a non-holonomic rolling constraint to account for pure rolling without slipping while constraining the solution space.

ACKNOWLEDGMENT

The authors would like to thank Chase Fortin for his help in fabricating several iterations of the prototype.

REFERENCES

- [1] K. G. Gim and J. Kim, “Ringbot: Monocycle Robot With Legs,” *IEEE Transactions on Robotics*, vol. 40, pp. 1890–1905,

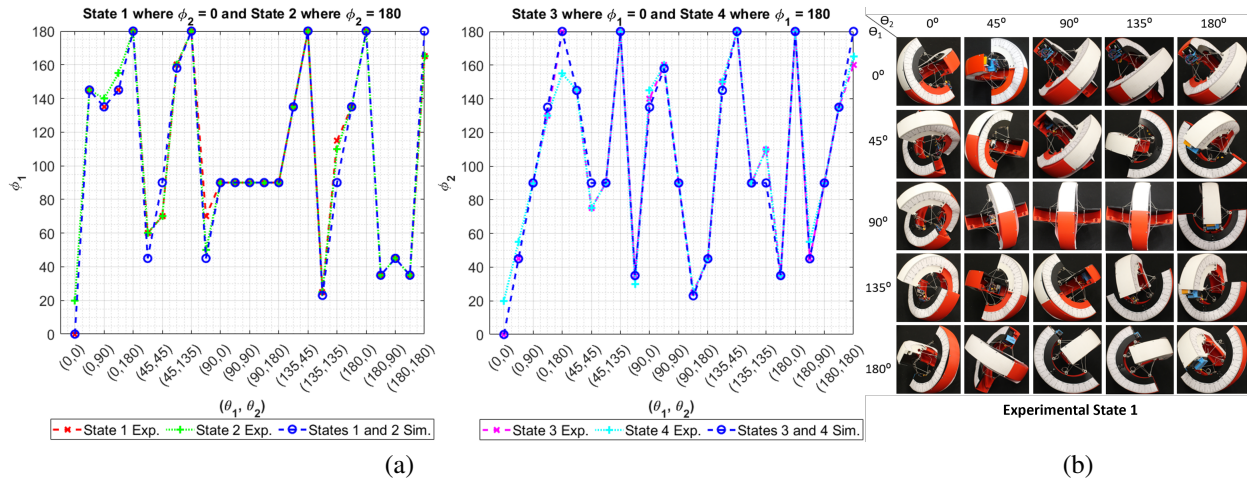


Fig. 10: Experimental static solutions are validated through incrementally varying (θ_1, θ_2) by 45° . (a) The experimental vs. simulated values for States 1- 4. (b) All overhead experimental results for State 1.

- 2024, conference Name: IEEE Transactions on Robotics. [Online]. Available: <https://ieeexplore.ieee.org/document/10423226>
- [2] U. Saranlı, M. Buehler, and D. E. Koditschek, "Rhex: A simple and highly mobile hexapod robot," *The International Journal of Robotics Research*, vol. 20, no. 7, pp. 616–631, 2001.
 - [3] R. D. Quinn, G. M. Nelson, R. J. Bachmann, D. A. Kingsley, J. T. Offi, T. J. Allen, and R. E. Ritzmann, "Parallel complementary strategies for implementing biological principles into mobile robots," *The International Journal of Robotics Research*, vol. 22, no. 3-4, pp. 169–186, 2003.
 - [4] R. Chase and A. Pandya, "A Review of Active Mechanical Driving Principles of Spherical Robots," *Robotics*, vol. 1, no. 1, pp. 3–23, Dec. 2012, number: 1 Publisher: Multidisciplinary Digital Publishing Institute. [Online]. Available: <https://www.mdpi.com/2218-6581/1/1/3>
 - [5] A. Morinaga, M. Svinin, and M. Yamamoto, "A Motion Planning Strategy for a Spherical Rolling Robot Driven by Two Internal Robots," *IEEE Transactions on Robotics*, vol. 30, no. 4, pp. 993–1002, Aug. 2014.
 - [6] T. Ohsawa, "Geometric Kinematic Control of a Spherical Rolling Robot," *Journal of Nonlinear Science*, vol. 30, no. 1, pp. 67–91, Feb. 2020. [Online]. Available: <http://link.springer.com/10.1007/s00332-019-09568-x>
 - [7] K. Snelson, "Snelson on the tensegrity invention," *International Journal of Space Structures*, vol. 11, no. 1-2, pp. 43–48, 1996.
 - [8] R. E. Skelton and M. C. De Oliveira, *Tensegrity systems*. Springer, 2009, vol. 1.
 - [9] C. Paul, F. Valero-Cuevas, and H. Lipson, "Design and control of tensegrity robots for locomotion," *IEEE Transactions on Robotics*, vol. 22, no. 5, pp. 944–957, Oct. 2006.
 - [10] A. P. Sabelhaus, J. Bruce, K. Caluwaerts, P. Manovi, R. F. Firoozi, S. Dobi, A. M. Agogino, and V. SunSpiral, "System design and locomotion of SUPERball, an untethered tensegrity robot," in *2015 IEEE International Conference on Robotics and Automation (ICRA)*. Seattle, WA, USA: IEEE, May 2015, pp. 2867–2873. [Online]. Available: <http://ieeexplore.ieee.org/document/7139590/>
 - [11] K. Caluwaerts, J. Despraz, A. İçen, A. P. Sabelhaus, J. Bruce, B. Schrauwen, and V. SunSpiral, "Design and control of compliant tensegrity robots through simulation and hardware validation," *Journal of The Royal Society Interface*, vol. 11, no. 98, p. 20140520, Sep. 2014. [Online]. Available: <https://royalsocietypublishing.org/doi/10.1098/rsif.2014.0520>
 - [12] L.-H. Chen, K. Kim, E. Tang, K. Li, R. House, E. L. Zhu, K. Fountain, A. M. Agogino, A. Agogino, V. Sunspirial, and E. Jung, "Soft Spherical Tensegrity Robot Design Using Rod-Centered Actuation and Control," *Journal of Mechanisms and Robotics*, vol. 9, no. 025001, Mar. 2017. [Online]. Available: <https://doi.org/10.1115/1.4036014>
 - [13] J. Rieffel and J.-B. Mouret, "Adaptive and resilient soft tensegrity robots," *Soft robotics*, vol. 5, no. 3, pp. 318–329, 2018.
 - [14] T. Rhodes, C. Gotberg, and V. Vikas, "Compact Shape Morphing Tensegrity Robots Capable of Locomotion," *Frontiers in Robotics and AI*, vol. 6, 2019. [Online]. Available: <https://www.frontiersin.org/articles/10.3389/frobt.2019.00111>
 - [15] V. Böhm, T. Kaufhold, F. Schale, and K. Zimmermann, "Spherical mobile robot based on a tensegrity structure with curved compressed members," in *2016 IEEE International Conference on Advanced Intelligent Mechatronics (AIM)*, Jul. 2016, pp. 1509–1514.
 - [16] V. Böhm, T. Kaufhold, I. Zeidis, and K. Zimmermann, "Dynamic analysis of a spherical mobile robot based on a tensegrity structure with two curved compressed members," *Archive of Applied Mechanics*, vol. 87, no. 5, pp. 853–864, May 2017. [Online]. Available: <https://doi.org/10.1007/s00419-016-1183-z>
 - [17] T. Kaufhold, F. Schale, V. Böhm, and K. Zimmermann, "Indoor locomotion experiments of a spherical mobile robot based on a tensegrity structure with curved compressed members," in *2017 IEEE International Conference on Advanced Intelligent Mechatronics (AIM)*, Jul. 2017, pp. 523–528, ISSN: 2159-6255.
 - [18] P. Schorr, E. R. C. Li, T. Kaufhold, J. A. R. Hernández, L. Zentner, K. Zimmermann, and V. Böhm, "Kinematic analysis of a rolling tensegrity structure with spatially fixed members," *Meccanica*, vol. 56, no. 4, pp. 953–961, Apr. 2021. [Online]. Available: <https://doi.org/10.1007/s11012-020-01199-x>
 - [19] M. Antali and G. Stepan, "Slipping-rolling transitions of a body with two contact points," *Nonlinear Dynamics*, vol. 107, no. 2, pp. 1511–1528, Jan. 2022. [Online]. Available: <https://doi.org/10.1007/s11071-021-06538-5>
 - [20] R. M. Murray, Z. Li, and S. S. Sastry, *A Mathematical Introduction to Robotic Manipulation*, 1st ed. CRC Press, Dec. 2017. [Online]. Available: <https://www.taylorfrancis.com/books/9781351469791>
 - [21] A. Tibert and S. Pellegrino, "Review of Form-Finding Methods for Tensegrity Structures," *International Journal of Space Structures*, vol. 18, no. 4, pp. 209–223, Dec. 2003, publisher: SAGE Publications Ltd STM. [Online]. Available: <https://doi.org/10.1260/026635103322987940>
 - [22] R. Connelly and W. Whiteley, "Second-Order Rigidity and Prestress Stability for Tensegrity Frameworks," *SIAM Journal on Discrete Mathematics*, vol. 9, no. 3, pp. 453–491, Aug. 1996. [Online]. Available: <https://doi.org/10.1137/S0895480192229236>
 - [23] C. Woods and V. Vikas, "Design and Modeling Framework for DexTeR: Dexterous Continuum Tensegrity Manipulator," *Journal of Mechanisms and Robotics*, vol. 15, no. 031006, Mar. 2023. [Online]. Available: <https://doi.org/10.1115/1.4056959>